16th World Conference on Earthquake, 16WCEE 2017
Santiago Chile, January 9th to 13th 2017
Paper N° 4890 (Abstract ID)
Registration Code: S-U1464683435

A SCREENING METHOD TO EXAMINE BEAM-END DAMAGE OF STEEL BRACED FRAME INCLUDING BRACE FRACTURE

R. Matsui[(1)], Y. Inaba[(2)], T. Takeuchi[(3)]

[(1)] Assistant Professor, Tokyo Institute of Technology, matsui.r.aa@m.titech.ac.jp
[(2)] Graduate Student, Tokyo Institute of Technology, inaba.y.ae@m.titech.ac.jp
[(3)] Professor, Tokyo Institute of Technology, ttoru@arch.titech.ac.jp

Abstract

Recently, there have been concerns of the risk of fracture at the beam-ends of existing steel building frames during the long period and long duration motion of the Nankai-trough great earthquake, which is expected in the near future. Researchers have proposed several simple evaluation methods to estimate cumulative damage from maximum ductility demand, avoiding the need for time history analysis. In this paper, cumulative damage at the beam-ends of a high rise steel building during long period and long duration motions is evaluated taking brace fracture into account. A simple damage evaluation method is proposed based on the event velocity and energy spectrum.

Keywords: Long Period Earthquake Motion, Braced Steel Frame, Member Fracture, Damage Evaluation

1. Introduction

The 2011 Tohoku Earthquake ruptured several asperities at the same time, which generated a large scale and long period ground motion. Recently, concerns have been raised of the risk of fracture at the beam-ends of existing steel building frames subjected to the long period and long duration motion caused by the Nankai-trough great earthquake, which is expected in near future [1], [2]. Particularly, existing concentrically braced frames (CBF) are expected to experience brace fracture, amplifying damages at the beam-ends. Up to now, Miner's rule has been one of the most popular linear cumulative damage rules for evaluating damage of these members. To assess damage of the beam-ends under random seismic waves, all the strain amplitudes in the random response history are generally required. However, calculating this cumulative strain demand using time history analysis is time consuming. To reduce the calculation effort, researchers have proposed several simple approaches to estimate the strain amplitude [3-8]. In this paper, several simple approaches for evaluating fracture of the beam-ends are examined and compared using an example of an 85 m height building.

The input ground motions were selected based on the maximum credible earthquake for several asperities in Japan, with a maximum duration of 655 s. The example structure is a 21 story high-rise building, constituted of a steel moment frame with regular circular hollow section braces (CHS) or buckling-restrained braces (BRBs). The natural period of the model with regular braces is 1.92 s, and that of the BRB model 2.48 s. Damage at the beam-ends is assessed by a method using ductility [3] or local strain [4-6]. Local strain is assessed by the rotational displacement of the beam-ends using a direct method, which is proposed by the authors. Based on this direct method, the calculations indicate that the beam-ends may fracture in the building model under the long period and strong ground motions [4-6].

Generally the frequency distribution of all strain amplitudes is required to access low cycle fatigue of steel materials. This requires time history analysis and Miner's rule. In this paper several simplified methods that only require the maximum ductility ratio are reviewed and compared. These methods assess damage using equivalent reference strain amplitude, while evaluated cumulative strain from just the maximum strain amplitude, calibrated from numerical studies of artificial and observed earthquake records. Finally, a new screening method is introduced based on the earthquake's velocity and energy spectra. This method is useful for rapid screening of the beam-ends in high-rise buildings including the effect of brace fracture.

2. Organization

2.1 Braced frame model

A typical steel braced frame as shown in Fig. 1 was modelled. The total height was 84.2 m, with the model with normal CHS braces denoted "CHS model" and that with BRBs as "BRB model". The building model was created as a planar model and Table 1 lists the building member dimensions and properties. Wide flange beams are connected to rectangular hollow section columns. The CHS braces were designed following the Japanese code (Ultimate strength design) [9], and the capacity of BRBs determined by calibrating each story drift angle of the BRB models to 1/100 rad [10]. The natural period of the CHS model is 1.92 s, and that of the BRB model is 2.48 s.

2.2 Member properties

The column and beam members were modelled with flexural beam elements, and the braces with truss elements. The beams are connected to the columns with rigid-plastic rotational springs, and the column base is fixed to the ground. Table 1 lists the yield forces, and the elastic modulus of the column and brace members was taken as 205,000 N/mm^2, and with 307,500N/mm^2 adopted for the beam members to account for the slab effect. The tangent modulus of the steel material after yielding was reduced to 1/100 times the elastic state, and buckling hysteresis behavior of the CHS members was calculated from the revised Shibata-Wakabashi model [11]. Newmark-Beta method was used to solve the time history response analysis model with the time increment = 0.01 s, and β = 1/4. For the BRBs, fracture was determined from [12], which considers the steel Bauschinger portions of the hysteresis loop. For, CHS, fracture was determined considering local strain amplification factors [13]. After fracture, the strength of the members decreases to zero, and the stiffness was reduced to 1/10000 the pre-fracture value.

2.3 Long period and long duration ground motions

Fig. 2 summarizes the velocity response spectra of the input ground motions. Each artificial ground motion was determined on the basis of the Nankai trough in Japan. The duration of the artificial motions was approximately 655 s, and that of the observed motions was 50 s. The Japanese code defined artificial ground motions were used [14], and the velocity response was categorized into three levels: 80m/s, 120m/s and 160m/s. Each symbol denotes the Metropolitan Area in Japan with CH for Chukyo, OS for Osaka, SZ for Shizuoka, and KA for Kanto. The observed ground motion was normalized by the velocity spectra in the Japanese code using the least square method. The dominant period of OS and KA is around 5 to 8 s, much greater than the example building model. By contrast, the dominant period of CH and SZ is shorter than OS and KA, and similar to the natural period of the building model, with the dominant periods ranging from 1 to 5 s for CH, and 1 to 3.5 s for SZ.

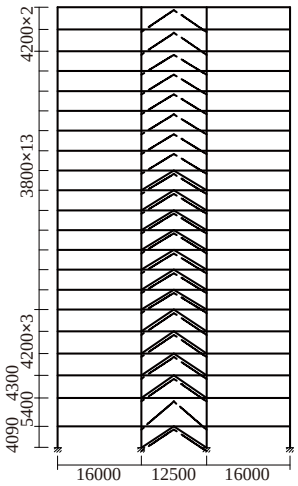

Fig. 1 - Steel braced frame model dimensions

Table 1 Building member dimensions and properties

Story	Column	Beam	BRB Yield Force (kN)	CHS
21F	□-600×28	H-900×300×16×22	-	ϕ-216.3×4.5
20F	□-600×28		-	ϕ-216.3×8.2
19F	□-600×32		-	ϕ-216.3×8.2
18F			-	ϕ-216.3×9.3
17F			-	ϕ-216.3×9.3
16F	□-600×32	H-900×300×16×22	-	ϕ-318.5×7.9
15F	□-600×36	H-900×300×16×30	-	ϕ-355.6×6.4
14F			-	ϕ-355.6×7.9
13F			7.6	ϕ-355.6×7.9
12F	□-600×36		166.7	ϕ-355.6×9.5
11F	□-600×40		247.8	ϕ-355.6×9.5
10F			377.2	ϕ-355.6×11.1
9F			495.7	ϕ-406.4×12.7
8F	□-600×40		598.3	
7F	□-600×50	H-900×300×16×30	555.7	
6F		H-900×300×16×32	827.1	ϕ-406.4×12.7
5F	□-600×50		935.0	ϕ-457.2×12.7
4F	□-600×55		876.1	ϕ-457.2×12.7
3F	□-600×55	H-900×300×16×32	494.7	ϕ-457.2×9.5
2F	□-600×700×55	H-1100×300×19×33	-	ϕ-457.2×9.5
1F	□-600×700×55	H-1100×300×19×33	486.7	ϕ-457.2×7.9
Grade	BCP325	SS400	LY225	STK400

Table 2 Ground motion properties

	Ground motion	Duration (s)	S_v (cm/s)		R_E	
			BRB	CHS	BRB	CHS
Artificial wave						
CH1	Chukyo	655.34	161	149	2.89	2.87
CH2			114	124	2.64	2.67
CH3			88	80	1.70	2.58
OS1	Osaka		104	111	2.18	3.39
OS2			97	90	1.71	2.98
OS3			78	66	2.20	2.69
SZ1	Shizuoka		174	154	1.60	2.01
SZ2			113	118	1.88	2.18
SZ3			73	76	1.98	1.64
KA1	Kanto		39	34	3.03	2.68
Observed Wave						
ELC	El Centro NS	53.74	170	128	1.10	1.61
HCH	Hachinohe NS	50.98	210	129	1.90	1.90

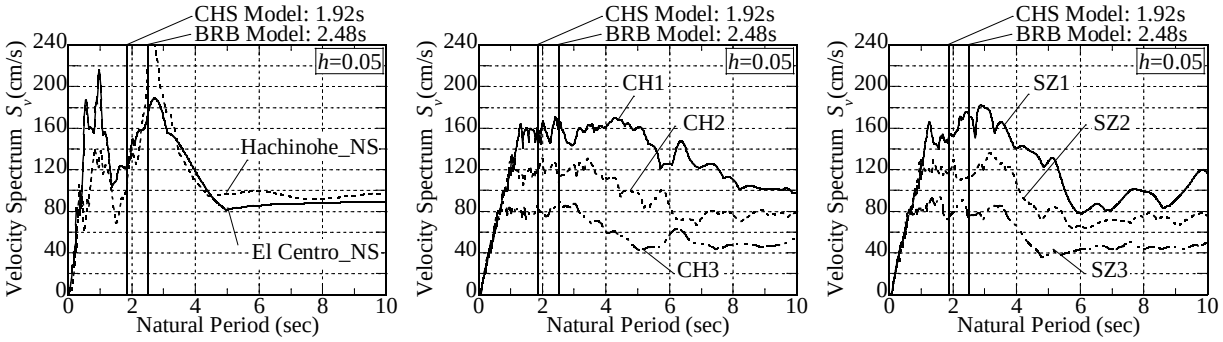

(a) Observed (b) CH (c) SZ

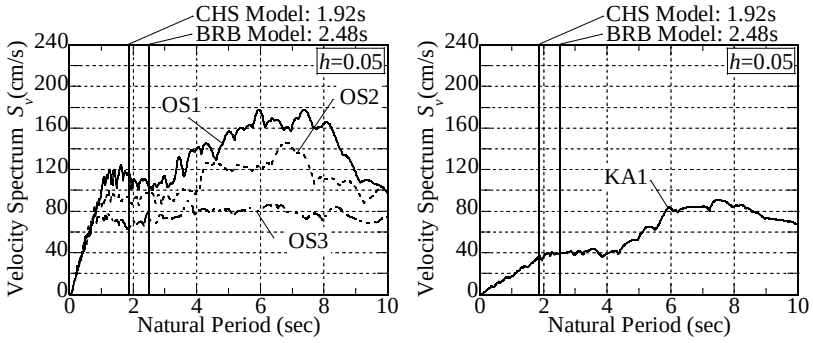

(d) OS (e) KA

Fig. 2 - Input ground motions

2.4 Beam-end damage in terms of time duration

In this section, the beam-end damage is assessed using the ductility ratio of the beam-end rotational angle using Miner's rule. The ductility ratio amplitudes are categorized into plastic and elastic regions.

Figs. 3 (a) and (b) depict the collapse mechanism, maximum story drift angle and damage distribution under the CH1 and HCH ground motions, without considering brace member fracture. Figs. 4 (a) and (b) show the results under the CH1 and HCH ground motions including the brace member fracture. The damage distribution in these figures follows a similar trend as the peak story drift. Brace fracture has a pronounced effect on the maximum beam-end damage, which is approximately 4 times greater than when fracture is neglected. The beam-end damage with a weld access hole is 2 - 3 times that with no weld access hole. Figs. 5 (a) and (b) illustrate the damage distribution of the BRB models considering the brace member fracture. The brace members in the CHS models often fracture, while these in the BRB models do not. The beam-end damage in the BRB models is around 1/3 ~ 1/4 times the CHS models.

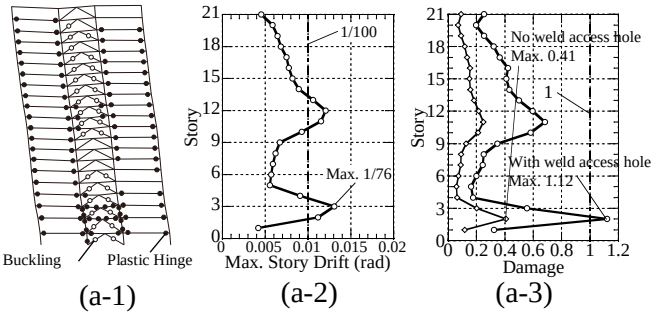

(a-1) (a-2) (a-3)

(a) CH1 ground motion

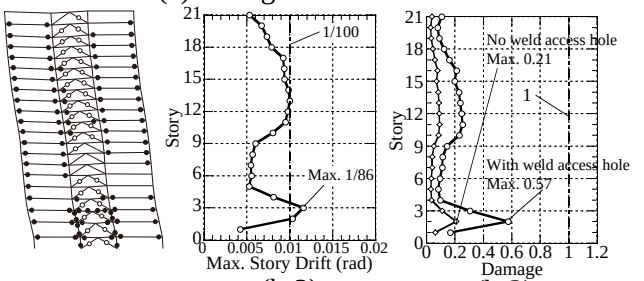

(b-1) (b-2) (b-3)

(b) HCH ground motion

Fig. 3 CHS Model Response
(Without considering brace fracture)

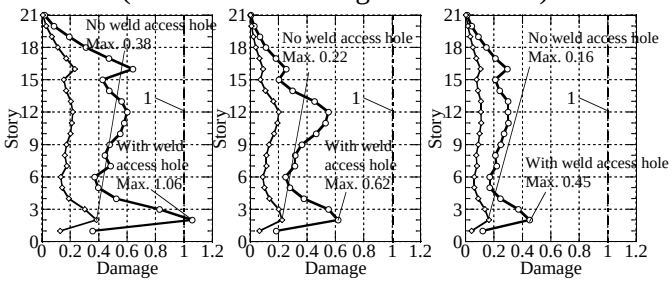

(a) CH1 (b) HCH (c) SZ1

Fig. 5 BRB Model Response
(Without considering brace fracture)

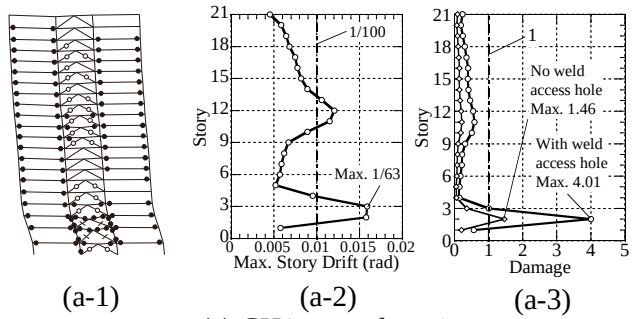

(a-1) (a-2) (a-3)

(a) CH1 ground motion

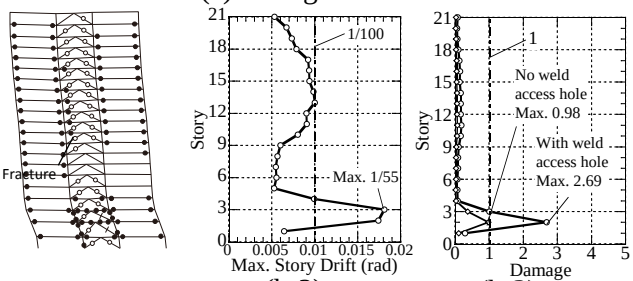

(b-1) (b-2) (b-3)

(b) HCH ground motion

Fig. 4 CHS Model Response
(Including brace fracture)

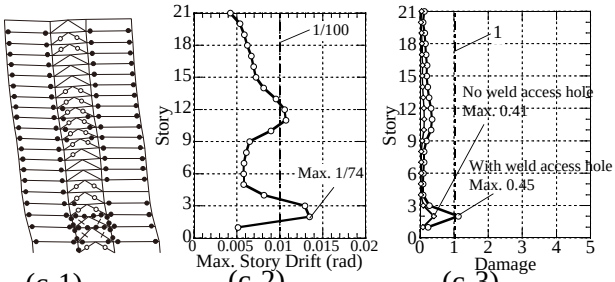

(c-1) (c-2) (c-3)

(c) SZ1 ground motion

Figs. 3 - 5 show that the beam-end damage under the far longer duration CH1 ground motion is larger than that under the HCH ground motion, which indicates that the time duration of the ground motion is a key parameter of the intensity of beam-end damage.

2.5 Beam-end damage in terms of frequency characteristics

Figs. 4 (a) and (c) represent the collapse mechanism, maximum story drift angle and damage distribution in the CHS models under the CH1 and SZ1 ground motions. The time duration and the maximum story drift of the CH1 ground motion is almost the same as that for the SZ1 ground motion. However, the beam-end damage of the CH1 is 4 times greater. Fig. 6 shows the 3rd story drift response at key time intervals, with the response to the CH1 and SZ1 motions approximately equal through the first 160s. The brace member buckling occurs around 122 - 157 s under both two ground motions, and after 160 s the response to SZ1 is smaller than for CH1. A potential explanation is that the equivalent period after yielding of the members is almost twice the elastic natural period, lengthening to 4 - 5 s. The dominant period of the CH1 ground motion ranges from 4 - 5 s, while the dominant period for SZ1 is shorter. Thus, the yielding of the members results in a longer period, resulting in the difference in response between the two motions.

3. Accuracy of beam-end damage evaluation proposed by previous researchers

Hasegawa et al. proposed a method (based on Manson-Coffin curves) to evaluate the beam-end damage using Eqs. (1) and (2).

$$\mu = C \cdot N_f^{-\beta} \tag{1}$$

$$\mu = \frac{\theta}{\theta_y} \tag{2}$$

where, μ is the ductility ratio, N_f is the fracture cycle, θ is the rotational angle, θ_y is the yield rotational angle, C is a coefficient (with access hole: 4.0; with no access hole: 5.6), and β is a constant value taken as 1/3 [3]. Whilst the authors have previously proposed another method (direct method), in the current method local strain $\Delta\varepsilon_l$ at beam end is calculated by an amplification factor (strain concentration ratio) and compared directly to the material fatigue performance curve Eq. (3) to determine the instant of fracture.

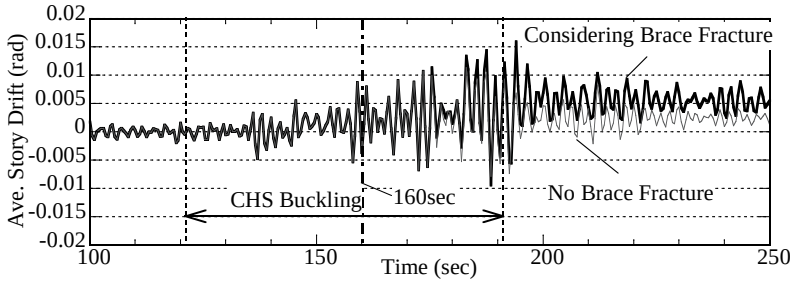

(a) CH1

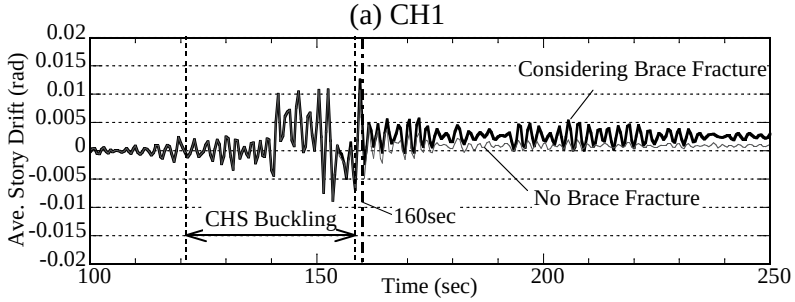

(b) SZ1

Fig. 6 Average story drift angle transition

$$\Delta\varepsilon_s = C_2 \cdot N_f^{-m_2} \tag{3}$$

where, $\Delta\varepsilon_s$ is the strain of steel material, coefficients C_2 = 35, and m_2 = 0.47 [15]. The local strain $\Delta\varepsilon_l$ is evaluated by Eqs. (4) - (6).

$$\Delta\phi_p = \alpha(2\Delta\theta_p)^{\beta_b}$$
$$\begin{cases} \alpha = \dfrac{1}{\sqrt{e_t L_{eq}}}\left(C_{\alpha 1}\dfrac{\sigma_y L_{eq}}{Eh} + C_{\alpha 2}\right) \\ \beta_b = C_{\beta 1}\left(C_{\beta 2} e_t\right)^{\left(-C_{\beta 3}\frac{\sigma_y L_{eq}}{Eh} + C_{\beta 4}\right)} \end{cases} \tag{4}$$

$$\Delta\varepsilon_n = \frac{h}{2}\left(\frac{\Delta M_c}{EI} + \Delta\phi_p\right) \tag{5}$$

$$\Delta\varepsilon_l = \min\left\{\max\left(\alpha_1\Delta\varepsilon_n, \alpha_2\Delta\varepsilon_n + \beta_2\right), \alpha_3\Delta\varepsilon_n + \beta_3\right\}$$
$$\begin{cases} \alpha_1 = -2.37\times10^{-3}\times\gamma_w + 4.31 \\ \alpha_2 = \exp(-1.66\times10^{-2}\times\gamma_w + 4.45) \\ \alpha_3 = -5.91\times10^{-2}\times\gamma_w + 8.66 \end{cases} \quad \begin{cases} \beta_2 = 4.23\times10^{-2}\times\gamma_w - 3.96 \\ \beta_3 = -2.25\times10^{-1}\times\gamma_w + 22.22 \end{cases} \tag{6}$$

$\Delta\theta_p$ is plastic rotational angle amplitude at the beam-end, $\Delta\phi_p$ is the plastic curvature amplitude at the beam-end, e_t is the strain hardening ratio of the steel material, L_{eq} is the beam equivalent length, h is the beam depth, σ_y is the yield stress, I is the beam's moment of inertia, ΔM_c is bending moment amplitude, γ_w is the joint efficiency, and $\Delta\varepsilon_n$ is the average strain amplitude at the beam-end. The other constant values are listed in Table 3. The fatigue performance curves calculated with the Manson-Coffin method (Eq. (1)) and direct method (Eq. (3)) are compared in Fig. 7. The fracture cycle calculated by Eq. (3) is larger than Eq. (1) for ductility ratios from 1.0 ~ 2.0, approximately equal for ductility ratios from 2.0 ~ 3.0, and is smaller for ductility ratios larger than 3.0. The coefficients of Eq. (6) are determined by numerical calculations, while those of Eq. (1) are determined by testing results. Eq. (7) is calculated by reformulate, Eqs. (1) and (3) instead of N_f. By setting these equations equal to each of the local strain as a function of μ is determined to substitute $\Delta\varepsilon_n$ for μ. Analytical expressions were developed and the results curve fitting to produce Eq. (7) with the coefficient listed in Table 3.

$$\Delta\varepsilon_l = \begin{cases} \min(A_{l1}\Delta\varepsilon_n^3 + B_{l1}\Delta\varepsilon_n^2 + C_{l1}\Delta\varepsilon_n, \\ \qquad A_{l2}\Delta\varepsilon_n^3 + B_{l2}\Delta\varepsilon_n^2 + C_{l2}\Delta\varepsilon_n + D_{l2}) & (\Delta\varepsilon_n \le 0.4\%) \\ A_{l2}\Delta\varepsilon_n^3 + B_{l2}\Delta\varepsilon_n^2 + C_{l2}\Delta\varepsilon_n + D_{l2} & (\Delta\varepsilon_n > 0.4\%) \end{cases} \tag{7}$$

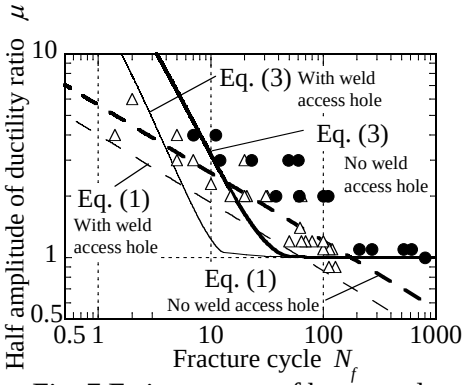

Fig. 7 Fatigue curve of beam-end

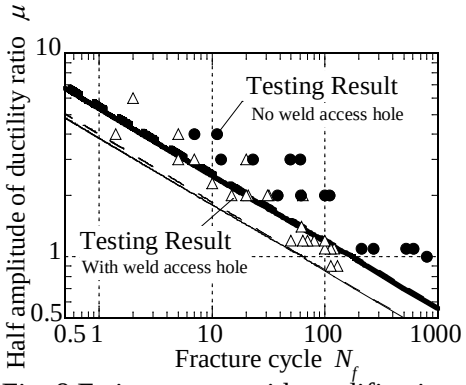

Fig. 8 Fatigue curve with modification

The revised fatigue performance curves using Eq. (7) are consistent with those calculated using the Manson-Coffin method (Eq. (1)), as shown in Fig. 8. The average strain is compared with the local strain at the beam-end in Fig. 9. The local strain calculated by Eq. (6) is similar to that by Eq. (7) in the elastic region, but in the plastic range Eq. (6) deviates from Eq. (7).

4. Reference ductility ratio for damage evaluation

4.1 Maximum and distributed reference ductility ratio

Miner's rule was used in the previous section, which requires time history analysis. Hasegawa et al. introduced two reference ductility ratios to evaluate the beam-end fracture, which do not necessarily require time history response analysis. The first method (M-Max) requires the maximum ductility ratio $\mu_{\max}$ calculated from the beam-end response. An equivalent cycle $n_{\max}$ is then calculated using the cumulative and peak ductility ratios shown in Fig. 10(a). Damage at the beam-ends is evaluated from the peak and equivalent ductility ratio and Eq. (8).

$$D = \frac{n_{\max}}{N_{f\max}} = \left\{ \frac{\eta}{4(\mu_{\max}-1)} \middle/ \left(\frac{\mu_{\max}}{C} \right)^{-\frac{1}{\beta}} \right\} = \frac{\eta}{4(\mu_{\max}-1)} \left(\frac{\mu_{\max}}{C} \right)^{\frac{1}{\beta}} \tag{8}$$

Where, N_f is the fracture cycle calculated from Eq. (2), and η is the cumulative ductility ratio. In the second method (M-Dist), the frequencies for each ductility ratio are converted into a uniform distribution as shown in Fig. 10(b). Damage at the beam-ends is then evaluated using Miner's rule and Eq. (9).

Table 3 Coefficient values

Eq. (4)	C_{a1}	C_{a2}		
	15	0.14		
	C_{b1}	C_{b2}	C_{b3}	C_{b4}
	0.61	14	2.0	0.038
Eq. (7)	A_{l1}	B_{l1}	C_{l1}	
With weld access hole	-223.29	137.91	10.77	
No weld access hole	-138.94	85.82	6.7	
Eq. (7)	A_{l2}	B_{l2}	C_{l2}	D_{l2}
With weld access hole	1.02	5.64	-0.61	4.82
No weld access hole	0.63	3.51	-0.38	2.99

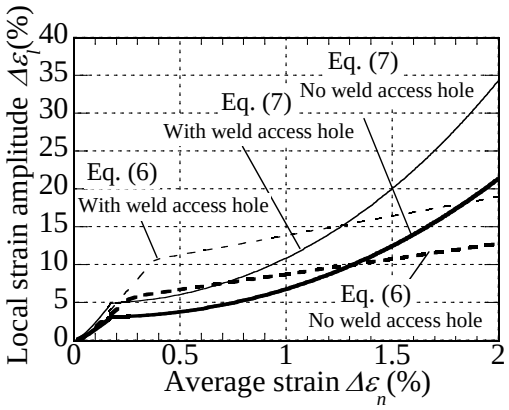

Fig. 9 Local strain at beam-end

$$D = \frac{\eta \cdot \mu_{\max}}{2\left(1+1/\beta\right)\left(\mu_{\max}-1\right)^2}\left(\frac{\mu_{\max}}{C}\right)^{\frac{1}{\beta}} \tag{9}$$

The damage indexes of the beam-ends calculated by time history response analysis are compared to those from the M-Max and the M-Dist methods in Fig. 10. The values calculated by the M-Max are typically larger than those by the M-Dist.

4.2 Alternative reference ductility ratio

In this section an alternative simple method (M-Ref) is proposed, where the time history of the ductility ratio is converted into a reference ductility ratio μ_{ref}. In this case, damage at the beam-ends D_{ref} is evaluated using Eq. (1) as follows:

$$D_{ref} = \frac{n_{ref}}{N_{f,ref}} = \left(\sum n_i \mu_i\right) \mu_{ref}^{\ -1+1/\beta} C^{-1/\beta} \tag{10}$$

Where, n_{ref} and $N_{f,ref}$ are the equivalent cycle and fracture cycle of the reference ductility ratio μ_{ref} respectively, and n_i is the number of cycles for each reference ductility ratio μ_i. On the other hand, the damage D_M at the beam-ends calculated by Miner's rule, is expressed by Eq. (11):

$$D_M = \sum \frac{n_i}{N_{fi}} = C^{-1/\beta} \sum n_i \mu_i^{1/\beta} \tag{11}$$

When the value of damage calculated by Eq. (10) is equal to that by Eq. (11), the coefficient γ is calculated as follows:

$$\gamma = \frac{\mu_{ref}}{\mu_{\max}} = \frac{1}{\mu_{\max}}\left(\frac{\sum n_i \mu_i^{1/\beta}}{\sum n_i \mu_i}\right)^{\frac{\beta}{1-\beta}} \tag{12}$$

Fig. 11 shows the frequencies of the ductility ratios for the CHS model under the SZ1 or the SZ2 ground motions. The frequencies are distributed continuously up to a certain ductility ratio, at which point several extreme values are observed. The ductility increment to the peak extreme value is denoted as ξ, which increases with the maximum velocity of the ground motion, as shown in Fig. 12. These characteristics are confirmed in the results from the full suite of ground motions. The frequency distribution parameters n and ξ are defined as a function of the ductility ratio as follows:

$$n(\mu) = A / \mu \tag{13}$$

$$\xi(\mu_{\max}) = \begin{cases} a\mu_{\max} - b & (\mu_{\max} \geq b/a) \\ 0 & (\mu_{\max} < b/a) \end{cases} \tag{14}$$

Where, A, a and b are constant values. The summations $\Sigma n_i\mu_i$ and $\Sigma n_i\mu_i^{1/\beta}$ in Eq. (12) are reformulated as integrals in Eqs. (15) and (16) respectively.

$$\int_0^{\mu_{\max}'} n(\mu)\mu d\mu + n(\mu_{\max})\mu_{\max} d\mu = (\mu_{\max}' + d\mu)A \tag{15}$$

$$\int_0^{\mu_{\max}'} n(\mu)\mu^{1/\beta} d\mu + n(\mu_{\max})\mu_{\max}^{1/\beta} d\mu = A\left\{\beta(\mu_{\max}')^{1/\beta} + \mu_{\max}^{-1+1/\beta} d\mu\right\} \tag{16}$$

Thus, when Eq. (15) is equal to Eq. (16), the coefficient γ in Eq. (12) is denoted as follows:

$$\gamma = \frac{1}{\mu_{\max}} \left\{ \frac{\beta(0.35\mu_{\max} + 0.65)^{1/\beta} + \mu_{\max}^{-1+1/\beta} \times 0.01}{0.35\mu_{\max} + 0.65 + 0.01} \right\}^{\frac{\beta}{1-\beta}} \tag{17}$$

Where the constant values a = b = 0.65, and $d\mu$=0.01 were determined numerically. Fig. 13 shows the relationship between the coefficient γ and the maximum ductility ratio $\mu_{\max}$. The coefficient γ decreases as the maximum ductility ratio $\mu_{\max}$ increases. Fig. 14 shows D-$\mu_{\max}$ relationship, which indicates that the damage D is frequently smaller than the maximum ductility ratio $\mu_{\max}$. Here, two values (0.37 and 0.5) are adopted for the coefficient γ to confirm the accuracy of applying the reference ductility for evaluation of damage at the beam-ends. Those two values give a conservative estimate for damage at the beam-ends. Fig. 15 indicates that the error between the time history analysis versus the M-Ref method ranges from -25% to 35%, an improvement over the M-Max and the M-Dist methods.

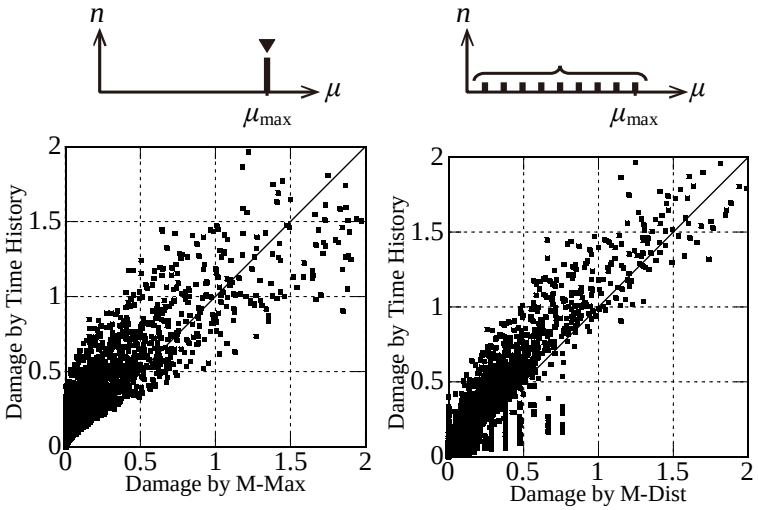

(a) M-Max (b) M-Dist

Fig. 10 M-Max and M-Dist Accuracy

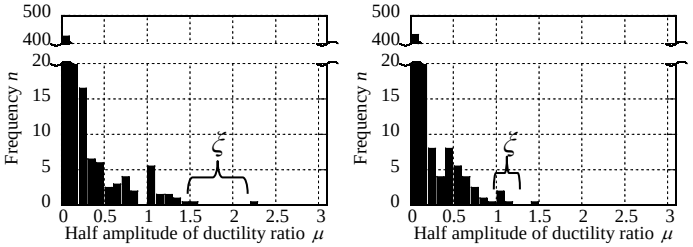

(a) CH1 (b) SZ1

Fig. 11 Frequency distribution of the ductility

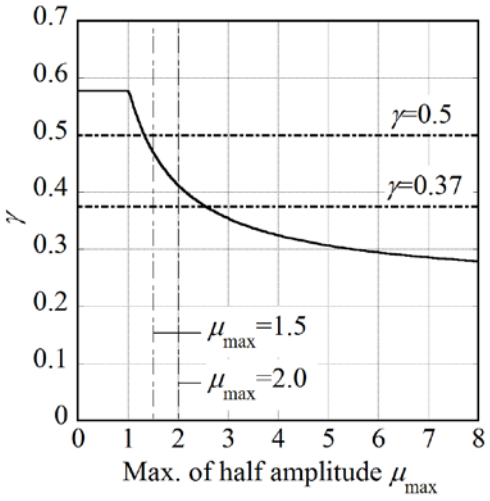

Fig. 13 γ-μ_{max} relationship

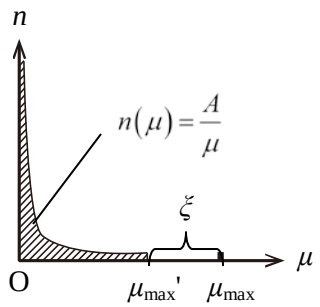

Fig. 12 Ductility ratio distribution model

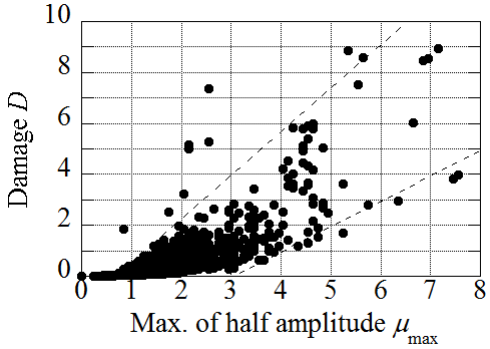

Fig. 14 D-μ_{max} relationship

5. Index for Screening Vulnerability of Beam-ends in Braced Steel Moment Frames

In this chapter, an evaluation method is proposed that does not require time history analysis nor maximum ductility to determine the beam-end damage. The energy ratio spectrum R_E is introduced, defined as the ratio of the earthquake energy spectrum V_E to the maximum velocity spectrum S_v, as shown in Eq. (18).

$$R_E(T) = \frac{V_E(T)}{S_v(T)} \tag{18}$$

In this study, damping is assumed as 5%. Fig. 16 represents the energy ratio R_E spectrum. When the natural period is larger than 4.0 sec, R_E of the artificial ground motion KA1, SZ1, CH1 and OS1 is larger than that of the observed ground motion ELC or HCH. The vertical axis of Fig. 17 shows that the maximum damage in all beam-end of the CHS model (with weld access holes) taking brace fracture into account. The maximum damage increases as the maximum velocity spectrum S_v increases, as shown in Fig. 17(a). When the maximum velocity is close to 160 cm/s and the R_E ranges from 2.0 to 3.5, the beam-ends are likely fracture as shown in Fig. 17(b).

The proposed value for R_E is only valid for the example building used in this study. For general application, further calibration for a broader range of building types is required. Once calibrated against a larger set of buildings, this method will be an effective means to screen damage at beam-ends, without resorting to time history response analysis.

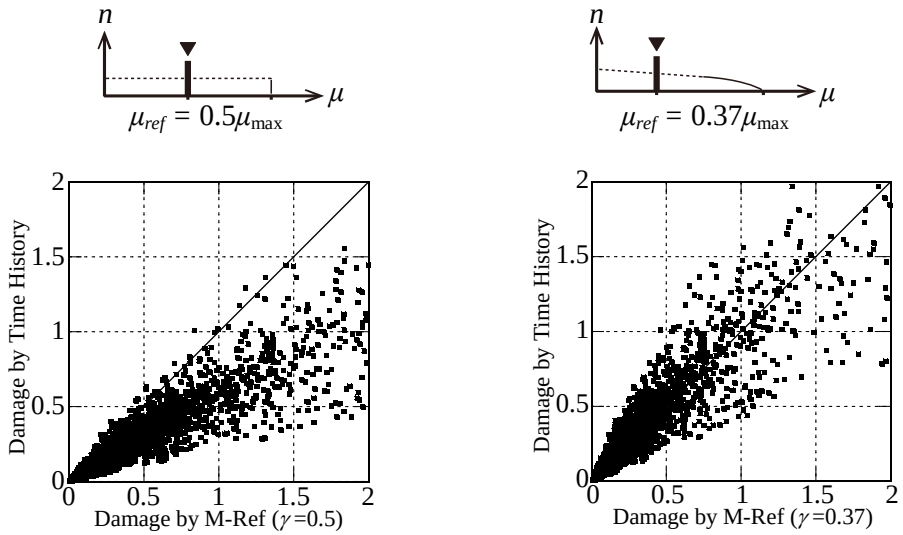

(a) γ=0.5 (b) γ=0.37

Fig. 15 M-Ref Accuracy

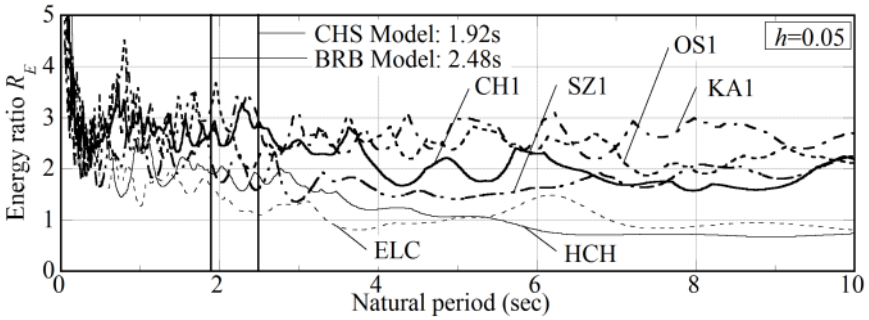

Fig. 16 Energy ratio spectrum

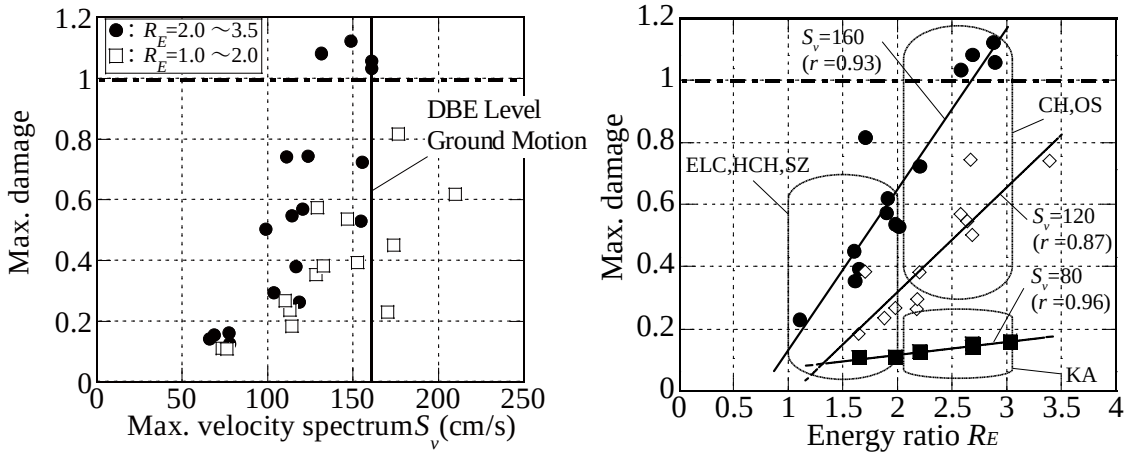

(a) Max. Damage - S_v (b) Max. Damage - R_E

Fig. 17 Relationship between max. damage and S_v or R_E

6. Conclusions

This research investigated damage evaluation method beam-ends in braced steel moment frames subjected to a long period and long duration motion. The results are summarized as follows.

1) The damage distribution of the beam-ends is likely to be similar to the story drift distribution. The damage of the beam-end with a weld access hole is frequently larger than that with no hole.

2) Damage values of the beam-ends calculated by the reference ductility ratios are consistent with those by the time history response results with a margin of error of plus or minus 30%.

3) For the example building, when the maximum velocity is close to 160 cm/s and the R_E ranges from 2.0 to 3.5, the beam-ends are likely to fracture.

7. References

[1] Building Research Institute Incorporated Administrative Agency, Japan (2010):Study on the Safety Countermeasures for Super-High-Rise Buildings etc. against the Long-Period Earthquake Ground Motions, *Building Research Data*, **127** (in Japanese)

[2] Building Research Institute Incorporated Administrative Agency, Japan (2013): Study on Long-Period Ground Motions and Responses of Super-High-Rise Buildings Etc. -Proposal of Updated Empirical Equations for Long-Period Ground Motions and Evaluation of Responses of Super-High-Rise and Seismically Isolated Buildings under the Hypothetical Nankai-Tonankai-Tokai Connected Earthquakes- , *Building Research Data*, **144** (in Japanese)

[3] Building Research Institute Incorporated Administrative Agency, Japan (2014): Study on Seismic Performance for Super-High-Rise Steel Buildings against Long-Period Earthquake Ground Motions, **160** *Building Research Data* (in Japanese)

[4] Takeuchi T, Ohyama T, Ishihara T (2010) : Cumulative Cyclic Deformation Capacity of High-Strength Steel Frames with Energy Dissipation Braces -Seismic performance of high-strength steel frames with energy dissipation braces Part 1-, *Journal of Structural and Construction Engineering (Transactions of AIJ)*, **75**(9), 1671-1679 (in Japanese)

[5] Takeuchi T, Ohyama T, Matsui R : Cumulative Deformation Capacity Evaluation of High-Strength Steel Beam Ends Subjected to Cyclic Bending Moment -Seismic performance of high-strength frames with energy dissipation braces Part2-, *Journal of Structural and Construction Engineering (Transactions of AIJ)*, **76**(3), 695-702 (in Japanese)

[6] Matsui R, Hiroyama T, Takeuchi T (2013): Energy Dissipation Performance of Braced Frames Focusing on Beam End Fracture, *Steel Construction Engineering, Japanese Society of Steel Construction*, **79**(9), 11-18 (in Japanese)

[7] Matsui R, Urui S, Tokuno M, Takeuchi T (2014): Seismic Performance Assessment for Steel Frames Considering Fracture of Beams and Braces, *Journal of Structural and Construction Engineering (Transactions of AIJ)*, **80**(11), 1745-1754 (in Japanese)

[8] Matsui R, Takeuchi T (2011)：Energy Dissipation Performance of Braced Moment Frames Focusing on Brace Fracture, *Journal of Structural and Construction Engineering (Transactions of AIJ)*, **76**(7), 1337-1345 (in Japanese)

[9] Ministry of Land, Infrastructure, Transport and Tourism (2007): Ministry of Land, Infrastructure, Transport and Tourism Notification No. 622 (in Japanese)

[10] The Japan Society of Seismic Isolation (2003): Manual for Structural Design and Construction of Passive Controlled Structures, Chapter 4.3 (in Japanese)

[11] Takeuchi T, Kondo Y, Matsui R, Imamura A (2012)：Post-Buckling Hysteresis and Cumulative Deformation Capacity of Built-Up Member Braces with Local Buckling, *Journal of Structural and Construction Engineering (Transactions of AIJ)*, **77**(11), 1781-1790 (in Japanese)

[12] T. Takeuchi, M. Ida, S. Yamada, K, Suzuki (2008): Estimation of Cumulative Deformation Capacity of Buckling Restrained Braces, *Journal of Structural Engineering, ASCE*, **134**(5), 822-831

[13] T. Takeuchi, R. Matsui: Cumulative Cyclic Deformation Capacity of Circular Tubular Braces under Local Buckling (2011): *Journal of Structural Engineering, ASCE*, **137**(11), 1311-1318

[14] Ministry of Construction (2000)：Ministry of Construction Notification No. 1457

[15] Saeki E, Sugisawa M, Yamaguchi T, Mochiduki H, Wada A (1995): A Study on Low Cycle Fatigue Characteristics of Low Yield Strength Steel, *Journal of Structural and Construction Engineering (Transactions of AIJ)*, **472**, 139-147 (in Japanese)